The Astrophysical Journal Supplement Series, 165:173–187, 2006 July

A *CHANDRA* CATALOG OF X-RAY SOURCES IN THE CENTRAL 150 pc OF THE GALAXY

M. P. Muno,[1,2] F. E. Bauer,[3,4] R. M. Bandyopadhyay,[5,6] and Q. D. Wang[7,8]

Received 2005 December 20; accepted 2006 March 29

ABSTRACT

We present the catalog of X-ray sources detected in a shallow *Chandra* survey of the inner $2^\circ \times 0.^\circ8$ of the Galaxy and in two deeper observations of the Radio Arches and Sgr B2. The catalog contains 1352 objects that are highly absorbed ($N_{\rm H} \gtrsim 4 \times 10^{22}$ cm^{-2}) and are therefore likely to lie near the Galactic center ($D \approx 8$ kpc), and 549 less absorbed sources that lie within $\lesssim$6 kpc of Earth. On the basis of the inferred luminosities of the X-ray sources and the expected numbers of various classes of objects, we suggest that the sources with $L_{\rm X} \lesssim 10^{33}$ ergs s^{-1} that comprise $\approx$90% of the catalog are cataclysmic variables and that the $\approx$100 brighter objects are accreting neutron stars and black holes, young isolated pulsars, and Wolf-Rayet and O (WR/O) stars in colliding-wind binaries. We find that the spatial distribution of X-ray sources matches that of the old stellar population observed in the infrared, which supports our suggestion that most of the X-ray sources are old cataclysmic variables. However, we find that there is an apparent excess of $\approx$10 bright sources in the Radio Arches region. That region is already known to be the site of recent star formation, so we suggest that the bright sources in this region are young high-mass X-ray binaries, pulsars, or WR/O star binaries. We briefly discuss some astrophysical questions that this catalog can be used to address.

Subject headings: catalogs — Galaxy: center — X-rays: general

Online material: machine-readable table

1. INTRODUCTION

The exquisite sensitivity of the *Chandra X-Ray Observatory* has provided vast improvements in our understanding of faint, hard X-ray sources. *Chandra* observations of distant galaxies allow us to study the X-ray population at luminosities similar to those accessible in our own Galaxy with wide-field X-ray instruments like the *Rossi X-Ray Timing Explorer* All-Sky Monitor and the *BeppoSAX* Wide-Field Camera ($L_{\rm X} \sim 10^{36}$ ergs s^{-1}), while observations of our own Galaxy are sensitive to sources a million times fainter than found with previous wide-field surveys. One of the most dramatic products of this improvement in sensitivity are the *Chandra* observations of the Galactic center (Wang et al. 2002; Baganoff et al. 2003). Whereas previous imaging surveys identified dozens of X-ray sources against a background of bright Galactic diffuse emission (Watson et al. 1981; Pavlinsky et al. 1994; Predehl & Truemper 1994; Sidoli et al. 1999, 2001; Sakano et al. 2002), *Chandra* observations have revealed thousands of individual X-ray sources (e.g., Wang et al. 2002; Muno et al. 2003) and discrete, filamentary features (e.g., Lu et al. 2003; Yusef-Zadeh et al. 2004). This high concentration of X-ray sources is not surprising. The $2^\circ \times 0.^\circ8$ (300 pc $\times$ 125 pc for a distance of 8 kpc; McNamara et al. 2000) region centered on the Galactic center contains roughly 1% of the Galactic mass (Lauhardt et al. 2002). Moreover, unlike the Galactic bulge, star formation has occurred continuously in the central region of the Galaxy, as is strikingly illustrated by the $\gtrsim$60 ultracompact H II regions in the giant molecular cloud Sgr B2 (de Pree et al. 1998) and by three young, dense clusters of massive stars (the Arches, the Quintuplet, and the Central Parsec; Krabbe et al. 1995; Figer et al. 1999).

A wealth of questions can be addressed with *Chandra* observations and with subsequent comparisons to multiwavelength catalogs. For instance, a variety of studies of the synthesis of compact, accreting binaries have been designed to explain the large number of X-ray sources *Chandra* detects in the Galactic center, and the results constrain, for example, the amount of angular momentum dissipated in the common envelope phase (e.g., Pfahl et al. 2002; Belczynski & Taam 2004; Liu & Li 2006; Ruiter et al. 2006). *Chandra* also can detect outbursts from transient low-mass X-ray binaries (LMXBs) at much lower flux levels than are accessible with traditional wide-field X-ray surveys, which provides unique insight into the duty cycles and emission mechanisms of compact objects accreting at very low rates ($\dot{M} \lesssim 10^{-11}\ M_\odot$ yr^{-1}; e.g., King 2000; Wijnands et al. 2002b; Wijnands & Wang 2002; in't Zand 2005; Sakano et al. 2005). Combining *Chandra* and radio observations can be used to identify young stars with powerful winds, which helps to constrain the rate at which massive stars have formed recently in the Galactic center (Yusef-Zadeh et al. 2002; Law & Yusef-Zadeh 2004; Muno et al. 2006).

Several observational studies have discussed the population of X-ray sources in *Chandra* surveys of the Galactic center. Wang et al. (2002) presented images from shallow (12 ks) *Chandra* exposures of the $2^\circ \times 0.^\circ8$ around Sgr A*, and gave a general overview of the number of X-ray sources and the properties of the diffuse X-ray emission. Takagi et al. (2002) studied the properties of X-ray sources associated with H II regions in Sgr B2. Yusef-Zadeh et al. (2002) and Law & Yusef-Zadeh (2004) studied the X-ray emission from massive stars in several clusters, including the Arches and Quintuplet. Finally, Muno et al. (2003, 2004, 2005), presented a comprehensive study of the population of X-ray sources with $L_{\rm X} = 10^{31}$–10^{33} ergs s^{-1} that were discovered in a deep (625 ks) set of *Chandra* observations of the inner 25 pc around

[1] Department of Physics and Astronomy, University of California, Los Angeles, CA 90095; mmuno@astro.ucla.edu.
[2] Hubble Fellow.
[3] Columbia Astrophysics Laboratory, Columbia University, Pupin Laboratories, 550 West 120th Street, Room 1418, New York, NY 10027.
[4] Chandra Fellow.
[5] Department of Astrophysics, University of Oxford, Keble Road, Oxford OX1 3RH, UK.
[6] Department of Astronomy, University of Florida, 211 Bryant Space Science Center, Gainesville, FL 32611.
[7] Department of Astronomy, University of Massachusetts, Amherst, MA 01003; wqd@astro.umass.edu.
[8] Institute for Advanced Study, Einstein Drive, Princeton, NJ 08540.

TABLE 1
OBSERVATIONS OF THE CENTRAL $2^\circ \times 0.^\circ8$ OF THE GALAXY

Start Time (UT)	Sequence	Target	Exposure (ks)	Aim Point R.A. (J2000.0) (deg)	Aim Point Decl. (J2000.0) (deg)	Roll (deg)
2000 Aug 30 16:59:32	658	1E 1740.7−2942	9.2	265.97583	−29.75008	270.8
2000 Mar 29 09:44:36	944	SGR B2	97.5	266.78034	−28.44169	87.8
2000 Jul 7 19:05:19	945	GC ARC	48.8	266.58192	−28.87196	284.4
2001 Jul 19 10:01:48	2267	GCS 20	8.7	266.17150	−29.27337	283.8
2001 Jul 20 04:37:11	2268	GCS 21	10.8	265.98136	−29.17141	283.8
2001 Jul 16 02:15:50	2269	GCS 1	10.5	267.05495	−28.37576	283.8
2001 Jul 20 08:00:49	2270	GCS 22	10.6	266.24512	−29.54138	283.8
2001 Jul 16 05:35:55	2271	GCS 2	10.4	266.86502	−28.27455	283.8
2001 Jul 20 11:12:40	2272	GCS 23	11.6	266.05423	−29.43957	283.8
2001 Jul 18 00:48:28	2273	GCS 10	11.2	266.70988	−28.87565	283.8
2001 Jul 16 08:44:25	2274	GCS 3	10.4	266.67662	−28.17301	283.8
2001 Jul 20 14:41:10	2275	GCS 24	11.6	265.86371	−29.33729	283.8
2001 Jul 18 04:16:58	2276	GCS 11	11.6	266.51970	−28.77438	283.8
2001 Jul 16 11:52:55	2277	GCS 4	10.4	266.94061	−28.54231	283.8
2001 Jul 20 18:09:40	2278	GCS 25	11.6	266.12769	−29.70775	283.8
2001 Jul 18 07:45:28	2279	GCS 12	11.6	266.33020	−28.67281	283.8
2001 Jul 16 15:01:25	2280	GCS 5	10.4	266.75037	−28.44124	283.8
2001 Jul 20 21:38:10	2281	GCS 26	11.6	265.93652	−29.60557	283.8
2001 Jul 18 11:13:58	2282	GCS 13	10.6	266.59425	−29.04216	283.8
2001 Jul 21 01:06:39	2283	GCS 27	11.6	265.74584	−29.50315	283.8
2001 Jul 18 14:25:48	2284	GCS 14	10.6	266.40487	−28.94088	283.8
2001 Jul 16 18:09:55	2285	GCS 6	10.4	266.56112	−28.34029	283.4
2001 Jul 21 04:35:09	2286	GCS 28	11.6	266.00997	−29.87372	283.8
2001 Jul 18 17:37:38	2287	GCS 15	10.6	266.21439	−28.83925	283.8
2001 Jul 17 14:11:51	2288	GCS 7	11.1	266.82518	−28.70891	283.8
2001 Jul 21 08:03:39	2289	GCS 29	11.6	265.81855	−29.77165	283.8
2001 Jul 21 11:32:10	2290	GCS 30	11.6	265.62772	−29.66900	283.8
2001 Jul 18 20:49:28	2291	GCS 16	10.6	266.47839	−29.20880	283.8
2001 Jul 17 17:51:28	2292	GCS 8	11.6	266.63516	−28.60795	283.8
2001 Jul 19 00:01:18	2293	GCS 17	11.1	266.28794	−29.10740	283.8
2001 Jul 17 21:19:58	2294	GCS 9	11.6	266.44581	−28.50671	283.8
2001 Jul 19 03:21:28	2295	GCS 18	11.1	266.09836	−29.00518	283.8
2001 Jul 19 06:41:38	2296	GCS 19	11.1	266.36205	−29.37522	283.8

Sgr A*. However, aside from the inner 25 pc, no catalog containing all of the X-ray sources found within the inner 150 pc of the Galactic center has been published.

In this paper, we rectify this by reporting the locations and basic properties of the X-ray sources detected in *Chandra* observations of the inner $2^\circ \times 0.^\circ8$ around the Galactic center. In § 2.1, we present the locations of these X-ray sources (excluding the inner $8'$ covered by the catalog in Muno et al. 2003) in order to facilitate searches for multiwavelength counterparts. In § 2.2, we present the fluxes and basic spectral properties in order to constrain the origin of the X-ray emission and to serve as baseline measurements for future searches for transient sources. In § 3.1, we examine the spatial distribution of the X-ray sources to determine how they are related to the stellar population that is observed in the infrared. In § 3.2, we study the luminosity distribution of the X-ray sources and report variations in the relative numbers of bright sources that could be related to recent star formation.

2. OBSERVATIONS

The central 300 pc × 125 pc of the Galaxy has been observed on several occasions with the imaging array of the *Chandra* Advanced CCD Imaging Spectrometer (ACIS-I; Weisskopf et al. 2002). The entire region was surveyed with overlapping ≈12 ks observations (Wang et al. 2002), and one additional short observation was obtained centered on the LMXB 1E 1740.7−2942. Deeper observations were taken of the H II regions in the giant molecular cloud Sgr B2 (100 ks; Takagi et al. 2002), and the nonthermal radio features referred to as the Arches (50 ks of public data as of 2005 June; Law & Yusef-Zadeh 2004). We list each of these observations in Table 1 and present a mosaic image of the survey in Figure 1.

The ACIS-I is a set of four 1024 pixel × 1024 pixel CCDs, covering a field of view of $17' \times 17'$. When placed on-axis at the focal plane of the grazing-incidence X-ray mirrors, the imaging resolution is determined primarily by the pixel size of the CCDs, $0.''492$. The CCD frames are read out every 3.2 s, which provides the nominal time resolution of the data. The CCDs also measure the energies of incident photons within a calibrated energy band of 0.5–8 keV, with a resolution of 50–300 eV (depending on photon energy and distance from the read-out node). However, in most of the observations (all those except observations 658, 944, and 945), an event filter was employed on the satellite that removed X-rays with energies below 1 keV before the data was sent to the ground. For the purposes of this paper, the lack of 0.5–1.0 keV photons only affects very soft foreground sources, as we explain below.

We reduced the observations using standard tools from the CIAO package, version 2.3.01. We started with the level-1 event lists provided by the *Chandra* X-Ray Center (CXC), and removed

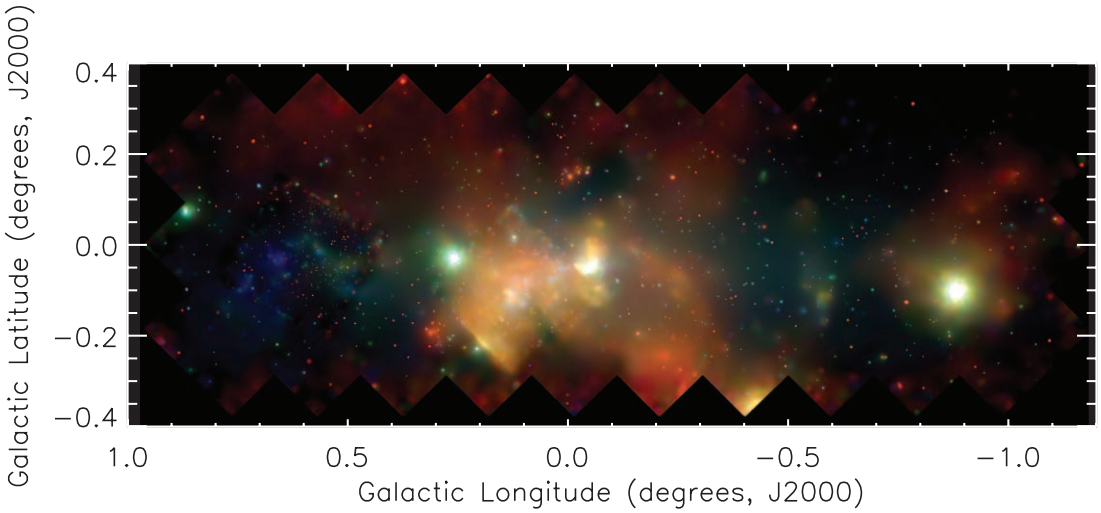

FIG. 1.—Mosaic image of the $0.^{\circ}8 \times 2^{\circ}$ field along the Galactic plane, centered on Sgr A*. The raw image has been adaptively smoothed with the CIAO tool `csmooth` for display purposes. The prominent features are the Sgr A complex at the center of the image, two bright X-ray binaries and their dust scattering halos at $l = 0.^{\circ}275$ and $-0.^{\circ}88$. Only a fraction of the brightest point sources are visible in this image. Note that the smoothing algorithm introduces significant artifacts, especially at the edges of the deep observations centered on Sgr B2 and the Arches.

the pixel randomization applied by the default processing software. We then modified the pulse heights of each event to partially correct for the position-dependent charge-transfer inefficiency caused by radiation damage early in the mission, using software provided by Townsley et al. (2002). We excluded most events flagged as possible background, but left in possible cosmic-ray afterglows because in the version of the processing software that we used they were difficult to distinguish from genuine X-rays from the strong diffuse emission and numerous point sources in the field. We applied the standard *ASCA* grade filters to the events, as well as the good-time filters supplied by the CXC. Finally, we searched each observation for time intervals when the detector background flared to $\geq 3\ \sigma$ above the mean level, and removed such intervals when they occurred (in observations 2267, 2269, 2273, 2288, and 944).

2.1. *Source Detection and Initial Localization*

We searched for X-ray sources separately in sets of nine images for each observation using the wavelet routine `wavdetect` (Freeman et al. 2002). We generated images in three energy bands: the full 1.0–8.0 or 0.5–8.0 keV (for observations 648, 944, and 945) band, the 1.0–2.0 or 0.5–8.0 keV band to increase our sensitivity to foreground sources, and the 4–8 keV band to increase our sensitivity to highly absorbed sources. For the purposes of source detection only, we removed events that had been flagged as possible cosmic-ray afterglows. We employed the default "Mexican Hat" wavelet, and used a sensitivity threshold of 10^{-7} that corresponds to the chance of detecting a spurious source per pixel if the local background is spatially uniform. We searched each energy band using a succession of three images centered on the aim point of each exposure: 1024×1024 images at the full *Chandra* resolution of $0.''5$, 1024×1024 images binned by a factor of 2 to a resolution of $1''$, and images of variable size that covered the entire ACIS-I exposure for each observation with a resolution of $2''$. We used wavelet scales that increased by a factor of $\sqrt{2}$: 1–4 for the $0.''5$ image, 1–8 for the $1''$ image, and 1–16 for the $2''$ image. This succession of three images and spatial scales was used for computational efficiency, and produced identical results as running the algorithm on a single, full-resolution image (as was done for the sensitivity calculations in Appendix A).

We merged the source lists by first combining the lists from the three images taken at different pixel scales for each observation, then combining the lists from the three energy bands, and finally combining the lists from each observation. Sources were identified as matches if the they fell within the average radius of the 90% encircled-energy contour for the point-spread function (PSF) for 4.5 keV photons at the position of the source. When duplicate sources were found in the list, we retained the positions from the list derived from the highest resolution images, either the finest pixel scale, the lowest energy band, or the observation in which the source was closest to the aim point. The resulting combined source list from the 33 observations contained 1901 unique sources, 225 of which were only detected in the soft band, and 382 of which were only detected in the hard band. On the basis of the sensitivity threshold for `wavdetect` (10^{-7}), we expect 2 spurious sources per field, or $\sim$70 in the entire survey.

We attempted to refine the astrometry for each observation by matching foreground X-ray sources detected in the soft band, many of which are likely to be K and M dwarf stars (Muno et al. 2003), to infrared sources in the Two Micron All Sky Survey (2MASS) catalog. For the two observations longer than 50 ks (Sgr B2 and the Arches), we found that there were $\approx$20 matches between the soft X-ray and 2MASS catalog within $5'$ of the aim point. By randomly shifting the relative positions of the two catalogs, we determined that, with 90% confidence, fewer than 25% of these matches should be random. Using these matches, we could derive the absolute astrometry of the *Chandra* pointing to within $0.''1$.

Unfortunately, the shorter observations were less sensitive and contained far fewer X-ray sources. Whereas the $\gtrsim$50 ks exposures contained $\approx$200 X-ray sources, the shorter exposures generally contained only a couple dozen. In general, $\leq$2 X-ray sources could be identified with 2MASS counterparts, which was insufficient to improve the pipeline astrometry. Therefore, starting with the fields adjacent to the deep exposures of Sgr A* (Muno et al. 2003), the Arches, and Sgr B2 and moving outward, we derived the astrometry by matching the `wavdetect` positions of the X-ray sources matched those of adjacent fields. Unfortunately, because most of the matches made in this way relied on X-ray sources detected $\gtrsim 6'$ off-axis, the statistical uncertainty on the `wavdetect`

TABLE 2
CATALOG OF POINT SOURCES WITHIN $2^\circ \times 0.^\circ8$ OF THE GALACTIC CENTER

Source (CXO J)	R.A. (J2000.0) (deg)	Decl. (J2000.0) (deg)	Uncertainty (arcsec)	ObsID	Offset (arcmin)	T_{exp} (ks)	C_{net}	P_{det}	HR0[a]	HR2	F_X (10^{-7} photons cm^{-2} s^{-1})	Flags[b]
174204.8−295004	265.52037	−29.83456	6.8	2290	11.3	11.6	$15.4^{+8.0}_{-6.9}$	0.00	$-0.52^{+0.39}_{-0.42}$	−9.00	60.2	f
174206.8−293634	265.52864	−29.60967	4.4	2290	6.4	11.6	$4.2^{+4.1}_{-2.7}$	0.25	−9.00	$1.00_{-0.76}$	22.8	...
174208.6−294437	265.53594	−29.74381	2.7	2290	6.5	11.6	$8.2^{+5.5}_{-4.0}$	0.27	$-1.00^{+0.50}$	−9.00	24.8	f
174210.5−293640	265.54378	−29.61127	1.4	2290	5.7	11.6	$14.4^{+6.8}_{-5.7}$	0.95	−9.00	$0.29^{+0.46}_{-0.45}$	64.7	...
174216.1−293757	265.56710	−29.63269	1.2	2290	3.9	11.6	$8.7^{+5.0}_{-4.5}$	0.81	$0.15^{+0.70}_{-0.73}$	−9.00	25.9	s
174216.1−293733	265.56743	−29.62600	1.1	2290	4.1	11.6	$11.6^{+5.8}_{-5.3}$	0.99	−9.00	$0.67^{+0.33}_{-0.34}$	57.0	...
174217.8−293716	265.57445	−29.62111	1.1	2290	4.1	11.6	$10.6^{+5.6}_{-5.0}$	0.97	$1.00_{-1.09}$	$-0.35^{+0.58}_{-0.55}$	36.0	...
174218.6−293932	265.57781	−29.65904	1.0	2290	2.7	11.6	$6.7^{+4.3}_{-4.0}$	0.94	$1.00_{-1.09}$	$0.20^{+0.80}_{-0.90}$	25.2	...
174219.3−294333	265.58049	−29.72611	1.8	2290	4.2	11.6	$4.5^{+3.8}_{-3.0}$	0.17	−9.00	$-1.00^{+0.74}$	14.1	...
174220.1−293527	265.58409	−29.59088	2.7	2290	5.3	11.6	$4.5^{+3.9}_{-3.0}$	0.06	$1.00_{-0.89}$	−9.00	13.5	...
174220.2−293905	265.58434	−29.65165	0.9	2290	2.6	11.6	10.9 ± 5.3	0.99	$-1.00^{+0.55}$	$1.00_{-0.87}$	36.9	f
174221.3−294251	265.58907	−29.71429	1.8	2290	3.3	11.6	$2.7^{+2.7}_{-2.3}$	0.02	−9.00	$-1.00^{+1.08}$	7.7	s
174221.4−294648	265.58922	−29.78008	2.9	2290	6.9	11.6	$8.6^{+5.3}_{-4.8}$	0.63	$1.00_{-1.13}$	$0.46^{+0.55}_{-0.64}$	40.4	...
174222.8−294119.....	265.59538	−29.68878	1.0	2290	2.0	11.6	$3.7^{+3.2}_{-2.8}$	0.34	−9.00	$-0.00^{+0.99}_{-0.98}$	14.2	...
174223.4−293951	265.59755	−29.66417	0.9	2290	1.7	11.6	$5.8^{+3.9}_{-3.7}$	0.69	−9.00	$-0.35^{+0.77}_{-0.65}$	20.6	...
174224.2−293412	265.60115	−29.57021	1.9	2290	6.2	23.2	$12.0^{+7.1}_{-5.3}$	0.53	$1.00_{-0.85}$	$-0.02^{+0.59}_{-0.56}$	29.7	...
174224.7−294334	265.60295	−29.72612	1.1	2290	3.6	11.6	$8.6^{+5.1}_{-4.4}$	0.73	$-0.01^{+0.99}_{-0.97}$	$-1.00^{+0.64}$	22.3	...
174227.5−292603	265.61493	−29.43424	1.3	2283	8.1	11.6	$66.5^{+13.9}_{-13.1}$	0.89	$-0.55^{+0.18}_{-0.18}$	$-0.20^{+0.76}_{-0.65}$	204.3	sf
174228.4−294158	265.61836	−29.69945	1.1	2290	1.8	23.2	$3.3^{+4.2}_{-3.0}$	0.11	−9.00	$-0.12^{+1.13}_{-0.88}$	10.1	...
174228.4−293432	265.61870	−29.57567	1.8	2290	5.7	23.2	$9.8^{+5.7}_{-5.4}$	0.09	$-1.00^{+0.42}$	$1.00_{-1.33}$	15.4	f
174228.5−293737	265.61904	−29.62707	0.9	2290	2.7	23.2	$7.8^{+5.8}_{-5.7}$	0.75	−9.00	$1.00_{-1.13}$	20.3	...
174230.1−293950	265.62544	−29.66400	0.8	2290	0.4	23.2	$4.3^{+5.1}_{-4.1}$	0.10	−9.00	−9.00	9.3	...
174230.3−294714	265.62667	−29.78728	3.0	2290	7.0	11.6	$8.6^{+5.4}_{-4.7}$	0.17	$1.00_{-0.92}$	$-1.00^{+0.51}$	24.3	...
174230.6−294321	265.62789	−29.72259	0.8	2290	3.1	23.2	$20.2^{+9.2}_{-7.7}$	0.99	$0.07^{+0.62}_{-0.54}$	$-1.00^{+0.98}$	46.9	...
174231.4−294337	265.63109	−29.72701	1.7	2290	3.4	23.2	<8.7	0.00	...	...	8.9	...
174235.8−292450	265.64932	−29.41405	3.9	2283	7.4	11.6	$7.4^{+5.2}_{-4.3}$	0.07	$0.19^{+0.81}_{-0.89}$	$-1.00^{+0.77}$	19.7	...
174236.7−294343	265.65331	−29.72874	0.9	2290	3.7	23.2	$15.3^{+7.6}_{-6.5}$	0.82	$-1.00^{+0.49}$	$-0.00^{+0.80}_{-0.79}$	25.1	f
174236.8−293825	265.65361	−29.64055	0.8	2290	2.2	23.2	$17.0^{+8.3}_{-6.5}$	0.99	$-1.00^{+1.42}$	$0.18^{+0.40}_{-0.50}$	38.1	...
174237.2−294801	265.65522	−29.80029	2.2	2289	8.7	23.2	$28.2^{+10.0}_{-8.7}$	0.41	$-0.32^{+0.30}_{-0.35}$	−9.00	58.6	...
174237.3−293045	265.65573	−29.51258	1.9	2283	4.7	11.6	$5.5^{+4.2}_{-3.4}$	0.46	$1.00_{-0.74}$	$1.00_{-1.14}$	22.6	...

NOTES.—Table 2 is published in its entirety in the electronic edition of the *Astrophysical Journal Supplement*. A portion is shown here for guidance regarding its form and content.

[a] Colors are defined according to $(h - s)/(h + s)$, where h and s are the net counts in high- and low-energy bands, respectively. For the soft color, h is in the 2.0–3.3 keV band, and s is in the 0.5–2.0 keV band. For the hard color, h is 4.7008.0 keV and s is 3.3–4.7 keV. Values are set to −9.000 if the 90% confidence intervals of both bands contain zero counts. Lower (upper) uncertainty values are set to −9.000 if the harder (softer) band is consistent with zero.

[b] Sources are flagged with "s" if there is short-term variability within an observation, "l" if there was long-term variability when comparing the flux in multiple observations, "c" if the source was confused with its neighbors in some observations so that the photometry was computed from a region enclosing <90% of the flux in the PSF, and "f" if the source was only detected below 2 keV.

positions of each X-ray sources was significant, and the corrected astrometry again was not significantly more accurate than the default pipeline values. Therefore, we expect that the astrometric frame will be accurate to $0.''6$ in 95% of cases.[9]

In Table 2, we list the refined positions and positional uncertainties (90% confidence), which include statistical and systematic terms. For the statistical positional error, we use the parameterization as a function of offset angle and count rate in equation (5) of Hong et al. (2005b). We combine the statistical errors in quadrature with $0.''6$ systematic uncertainties for the shallow observations, and assume negligible systematic uncertainties for observations 944 and 945. In Table 2, we also list the observation in which a source was detected in, the offset from the aim point of that observation (which is used in the uncertainty calculation), and the total live time each source was observed with. We omitted two bright, previously known LMXBs from the table (1E 1740.7−2942 and 2E 1743.1−2842), because they were badly saturated in our survey images, and their positions and properties are reported elsewhere (e.g., Martí et al. 2000; Porquet et al. 2003).

2.2. *Photometry*

We computed photometry for each source using the `acis_extract` routine from the Tools for X-Ray Analysis (TARA).[10] We extracted event lists for each source for each observation, using an extraction region designed to enclose a large fraction of the PSF. We used a PSF at a fiducial energy of 1.5 keV for sources detected only in the soft band (flagged with an "f" to indicate a possible foreground source in Table 2), while we used a larger extraction area corresponding to a PSF for 4.5 keV photons when sources were detected in the full or hard bands.

In most cases, we chose polygonal regions that matched the contours of 90% encircled energy from the PSF. However, if the 90% contours of the PSFs of two nearby sources overlapped, we generally used a region that corresponded to a smaller fraction of the PSF. We have flagged these sources as confused ("c") in Table 2. The smallest extraction region that we used matched the 70% encircled energy contour. However, because the PSF grows significantly as a function of off-axis angle, in many cases a source that appeared isolated when it was located on-axis in one observation was indistinguishable from its neighbors in images from

[9] See http://cxc.harvard.edu/cal/ASPECT/celmon.

[10] See http://www.astro.psu.edu/xray/docs/TARA.

adjacent, overlapping pointings. We found that no reasonable fraction of the PSF would isolate counts from sources more than 7′ off-axis whose 90% encircled-energy radii overlapped those of their neighbors, so we did not extract photometry from observations in which confused sources were >7′ off-axis. Fortunately, these sources always lay near the aim point of another observation (or else they could not have been detected in the first place), so we were still able to obtain photometry for them.

For each source and each observation, a background event list was extracted from a circular region centered on the point source, excluding from the event list counts in circles circumscribing the ≈92% contour of the PSF around any point sources. We found that this value struck a good balance between excluding counts from point sources and leaving enough counts in the image to determine the background. The sizes of the background regions were chosen such that they contained approximately 100 events for each observation. Less than 1% of the counts in the background regions were from point sources. We also computed the effective area function (ARF) at the position of each source for each observation using the CIAO tool `mkarf`.

The source and background event lists were used to compute photometry for each source in five energy bands: the full band of 1.0–8.0 keV (most observations) or 0.5–8.0 keV (658, 944, and 945); 1.0–2.0 keV or 0.5–2.0 keV; 2.0–3.3 keV; 3.3–4.7 keV; and 4.7–8.0 keV. These bands are identical to those used by Muno et al. (2003) for the catalog of X-ray sources within 25 pc of Sgr A*. The energy bands were chosen so that they sampled regions of the ARF with roughly constant areas, and so that the three high-energy bands each contained about one-third of the net counts from most sources. The net counts in each band were computed by subtracting the estimated background from total counts. The 90% uncertainty in the net counts in each of the five bands were computed through a Bayesian analysis, with the simplifying assumption that the uncertainty on the background was negligible (Kraft et al. 1991). When the 90% confidence interval on the net counts was consistent with 0, we considered the upper bound on the 90% confidence interval to be the upper limit.

A histogram of the number of sources as a function of net counts in the full band is displayed in Figure 2. Most sources were detected with 10–20 counts in two overlapping 12 ks observations. Therefore, most sources were only observed with ≈5 counts in each of the smaller energy bands. The net counts from 303 sources are consistent with zero at the 90% level. About 70% of these sources are flagged in Table 2 because their photometry could be unreliable for various reasons: some are detected only in the soft band where the background is lower, some are variable so that the mean flux is not meaningful, and some are confused with nearby sources. The remaining ≈90 sources are probably spurious, as we expected ≈70 spurious sources based on our detection threshold. We suspect we detected ≈20 more spurious sources than we expected because the background in our observations is ≈10 times larger than in the observations taken at high Galactic latitude with which `wavdetect` was calibrated. We keep these potentially spurious sources in the catalog for completeness. The net counts and 90% uncertainties (or upper limits) are listed in Table 2. These values are used to compute the probability of detecting each source given its location and exposure, which is also listed in the table. The Monte Carlo simulations used to estimate this probability are described in Appendix A.

We computed approximate photon fluxes (in units of photons cm^{-2} s^{-1}) for each source by dividing the net counts in each subband by the total live time (units of s) and the mean value of the ARF in that energy range (units of cm^2; note that this value incorporates variations in exposure due to chip gaps and dead columns).

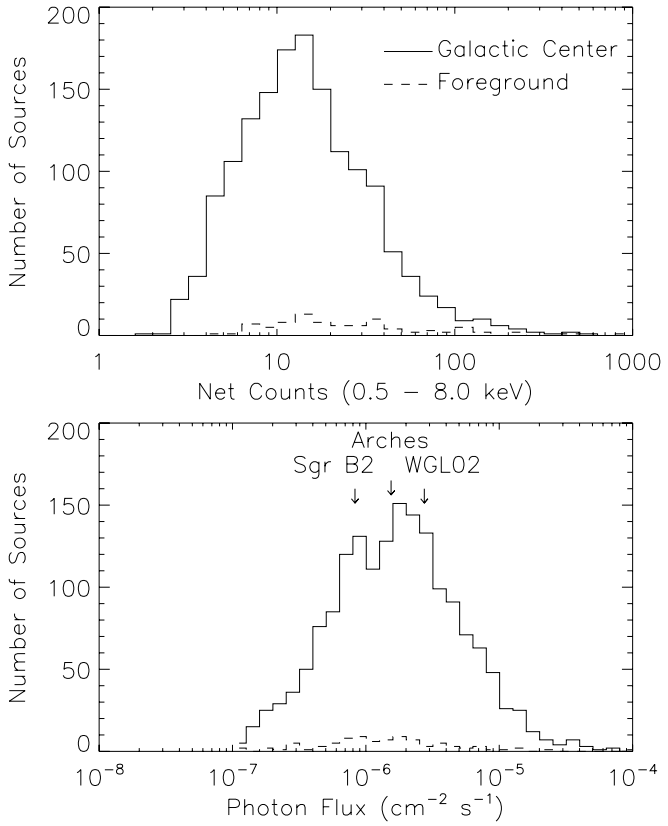

FIG. 2.—*Top*: Distribution in net counts from individual sources. No correction is applied to account for the exposure across the survey, which varies by a factor of 5. *Bottom*: Distribution of fluxes from individual sources, derived by dividing the net count rates by the effective area and exposure in four energy bands (0.5–2.0 keV [observations 658, 944, and 945] or 1.0–2.0 keV [see text]; 2.0–3.3 keV; 3.3–4.7 keV; and 4.7–8.0 keV), and summing the result. There are two peaks, because the deeper observations were more sensitive to faint sources. In both panels, the solid line is used for sources located near or beyond the Galactic center (HR > -0.175), and the dashed line for foreground sources (HR < -0.175). The arrows denote the median sensitivity for the shallow survey (labeled WGL02) and for the deep Arches and Sgr B2 fields.

The photon fluxes in the 0.5–8.0 keV energy band used throughout the paper are the sums of those in the subbands, using negative values when they occur (not the upper limits). They are listed in Table 2. The omission of photons below 1.0 keV in most of the observations probably caused us to underestimate the flux by $\lesssim$25% for the ≈150 sources that were only detected below 3.3 keV. However, none of these sources produced more than 38 net counts, and the mean number of net counts from these soft sources was 7, so this systematic uncertainty was generally comparable to that introduced by Poisson counting statistics. For the remaining sources, we also have found that the approximate photon fluxes that we computed differed from those derived from spectral fits by little more than the Poisson uncertainty in the count rate, because the energy bands sampled the ARF for the ACIS-I detector well (Muno et al. 2003).

A histogram of the number of sources as a function of the 0.5–8.0 keV photon flux is presented in the bottom panel of Figure 2. Galactic center sources are indicated with the solid line, and foreground sources with the dashed line (see below for the definitions of foreground and Galactic center sources). Sources are detected with average photon fluxes as low as 2×10^{-8} photons cm^{-2} s^{-1}. The largest number of Galactic center sources are detected near 2×10^{-6} photons cm^{-2} s^{-1} (2.0–8.0 keV), and the largest number of foreground sources are found near 1×10^{-6} photons cm^{-2} s^{-1} (0.5–2.0 keV).

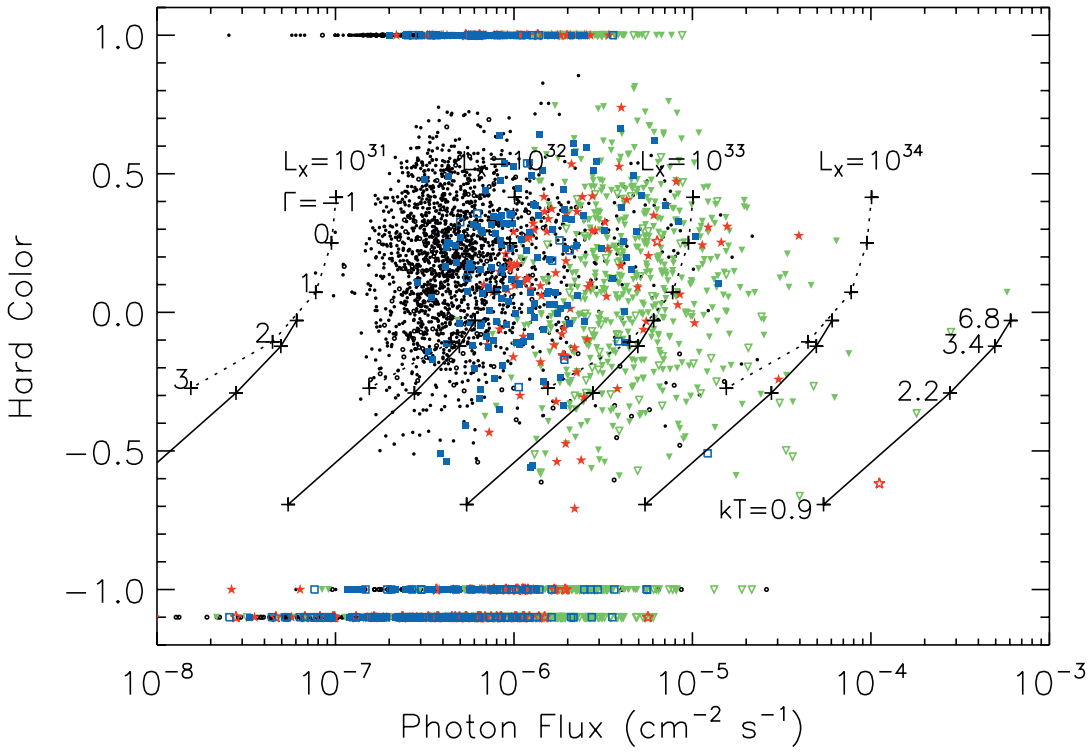

FIG. 3.—Hard color plotted against the photon flux from each source. The symbol shapes indicate which observations the sources were identified in: blue squares for the Sgr B2 field, red stars for the Arches region, and green triangles for the extended shallow survey. For comparison, we also include the data from the central 25 pc (Muno et al. 2003) using black circles. Open symbols indicate foreground sources, and filled circles those at or beyond the Galactic center (see text). Sources detected in only in the 3.3–4.7 keV band are assigned hard colors of −1; those only detected in the 4.7–8.0 keV band are assigned HR2 = +1, and those detected in neither band are assigned HR2 = −1.1. The uncertainties on the hard colors are significant. Sources with a probability of <50% of being detected have unreliable hard colors; those with a 50%–90% chance of detection have $\sigma_{HR2} \approx 0.6$; those with a 90%–99% chance of detection have $\sigma_{HR2} \approx 0.4$; and those with a >99% chance of detection have $\sigma_{HR2} \lesssim 0.3$. Finally, we have plotted the colors expected for sources of varying luminosities at a distance of 8 kpc, and absorbed by 6×10^{22} cm^{-2} of interstellar gas and dust. The dotted lines are for power-law spectra, and the solid lines for thermal plasma spectra. The sources with HR2 > 0.5 either have large uncertainties, large absorption columns, or both. For a fiducial conversion factor between photon flux and 0.5–8.0 keV luminosity, we assume a $\Gamma = 1.5$ power law or a $kT = 7$ keV plasma and find that 10^{34} ergs s^{-1} equals 6×10^{-5} photons cm^{-2} s^{-1}.

We used the counts in each energy band to compute two hardness ratios, which we used to characterize the absorption column toward each source and the steepness of the high-energy portion of each spectrum. The ratios are defined as the fractional difference between the count rates in two energy bands, $(h - s)/(h + s)$, where h and s are the numbers of counts in the higher and lower energy bands, respectively. The resulting ratio is bounded by −1 and +1. The soft color is defined by the fractional difference between counts with energies between 2.0–3.3 keV and 1.0–2.0 keV or 0.5–2.0 keV (HR0); and the hard color using counts between 4.7–8.0 keV and 3.3–4.7 keV (HR2; HR1 was defined in Muno et al. [2003] but was not useful for this paper). The hardness ratios are listed in Table 2, with uncertainties calculated according to equation (1.31) in Lyons (1991, p. 26).

We use simulated spectra to determine the mapping between the soft color (HR0) and the absorption column toward a source, and thereby to identify foreground and highly absorbed sources. The fact that most of the observations did not include <1 keV photons only affects the softest sources, with $N_H \lesssim 5 \times 10^{21}$ cm^{-2}. For instance, sources with $N_H \approx 10^{21}$ cm^{-2} will have HR0 < −0.5 using a 0.5–2.0 keV soft band, and HR0 < −0.3 using a 1.0–2.0 keV soft band. We find that regardless of whether or not <1 keV would have been retained, sources that have HR0 > −0.175 or that are not detected below 3.3 keV have absorption columns $N_H > 4 \times 10^{22}$ cm^{-2} and are therefore likely to lie at or beyond the Galactic center. We refer to these as the "Galactic center sources," of which there are 1350. The 549 sources with HR0 < −0.175 are considered foreground sources, because they are likely to be closer than 6 kpc.

In Figure 3, we plot the hard color versus the flux from each source. Foreground sources are indicated with open symbols, and sources at or beyond the Galactic center with filled symbols. There are 785 Galactic center sources and 39 foreground sources with measured hard colors. We have calculated the hardness ratios and photon fluxes that we would expect to get from these energy bands for a variety of spectra and 0.5–8.0 keV luminosities using PIMMS and XSPEC. In Figure 3, we plot the colors and fluxes expected for power-law spectra with the dotted lines, and for a optically thin thermal plasma with the solid lines. We have assumed a distance of 8 kpc and 6×10^{22} cm^{-2} of absorption from interstellar gas and dust. The median hard color for the Galactic center sources is 0.05. This corresponds to a $\Gamma = 1.5$ power law or a $kT = 1.7$ keV plasma spectrum.

The Galactic center sources in this survey are significantly softer than those from the deeper (limiting luminosity of $L_X = 2 \times 10^{31}$ ergs s^{-1}) catalog from the central 20 pc of the Galaxy. The latter catalog had a median hard color of 0.22 (Muno et al. 2003), corresponding to a $\Gamma = 0$ power-law spectrum. This suggests that the more luminous X-ray sources are systematically softer.

For a fiducial $\Gamma = 1.5$ spectrum absorbed by $N_H = 6 \times 10^{22}$ cm^{-2}, the photon fluxes can be converted to energy fluxes according to 1 photon cm^{-2} s^{-1} = 8×10^{-9} ergs cm^{-2} s^{-1} (0.5–8.0 keV). The deabsorbed 0.5–8.0 keV flux is approximately

3 times larger, so that for a distance $D = 8$ kpc, 10^{34} ergs s^{-1} equals 6×10^{-5} photons cm^{-2} s^{-1}. For sources detected below 2.0 keV, we find that 1 photon cm^{-2} s^{-1} $= 2 \times 10^{-9}$ ergs cm^{-2} s^{-1} between 0.5 and 2.0 keV. The absorption for these sources is relatively small ($<10^{22}$ cm^{-2}), and therefore so is the correction to derive an intrinsic flux.

3. RESULTS

3.1. *Spatial Distribution*

We examined the spatial distribution of the X-ray sources in order to determine how it compares to that of the ordinary stellar population observed in the infrared. We were most interested in sources near the Galactic center, so we only considered those sources with soft colors HR0 > -0.175. We also took care to select only sources that were bright enough to be detected over a large fraction of the survey. To do this, we derived maps of our sensitivity as described in Appendix A, and we examined only those sources that (1) were brighter than a well-defined flux limit, and (2) that were located at a position where the sensitivity was better than that flux limit. Our flux limit was designed so that sources brighter than the limit have at least a 50% chance of being detected over a significant fraction of our survey (see Appendix A for a description of the Monte Carlo simulations that we used to calculate the detection probability). We found that a flux limit of 3×10^{-6} photons cm^{-2} s^{-1} (equivalent to 5×10^{32} ergs s^{-1} [0.5–8.0 keV] taking $D = 8$ kpc, $N_{\rm H} = 6 \times 10^{22}$ cm^{-2}, and a $\Gamma = 1.5$ power law) provided the largest number of sources, 321 out of the 1899 sources in Table 2.

We then computed the surface density of sources as a function of offset from Sgr A* and of the absolute values of the Galactic latitudes and longitudes, and we plotted them in Figure 4. To account for the variations in our sensitivity over the survey region, the contribution of each source to the distribution was weighted by the inverse of the probability of detecting it (calculated as described in Appendix A). We used the catalog of Muno et al. (2003) to fill in the inner 8′ around Sgr A*. We used the identical flux cuts in the Sgr A* field as for the rest of the survey, which allowed us to include another 42 sources.

To compare the distribution of X-ray sources with that of the ordinary stellar population, we used models for the Galactic bulge and the central 150 pc that were derived from infrared maps by Launhardt et al. (2002), and the exponential model of the Galactic disk in Kent et al. (1991). These mass models are accurate to about 50%. We modeled the central 150 pc with two components. We assumed that the central 15 pc is dominated by a spherical cluster with a mass density profile

$$\rho = \frac{\rho_c}{1 + (r/r_c)^n}. \tag{1}$$

For $r < 6$ pc, we use $\rho_c = 3.3 \times 10^6\ M_\odot$ pc^{-3}, $r_c = 0.22$ pc, and $n = 2$. For 6 pc $< r <$ 200 pc, $n = 3$, r_c remains the same, and ρ_c is adjusted so that the function is continuous at $r = 6$ pc. The total mass of the central cluster is $6 \times 10^7\ M_\odot$.

The rest of the central 150 pc is dominated by a disklike distribution with a mass density

$$\rho = \rho_d r^{-n} \exp(-|z|/z_d). \tag{2}$$

For $r < 120$ pc, we take $\rho_d = 300\ M_\odot$ pc^{-3}, $n = 0.1$, and $z_d =$ 45 pc. For 120 pc $< r <$ 220 pc, we take $n = 3.5$, leave z_d the same, and adjust ρ_d so that the function is continuous at $r = 120$ pc. For 220 pc $< r <$ 2000 pc, we take $n = 10$ and treat the other parameters the same as above. The total mass of this nuclear stellar disk is $1.4 \times 10^9\ M_\odot$.

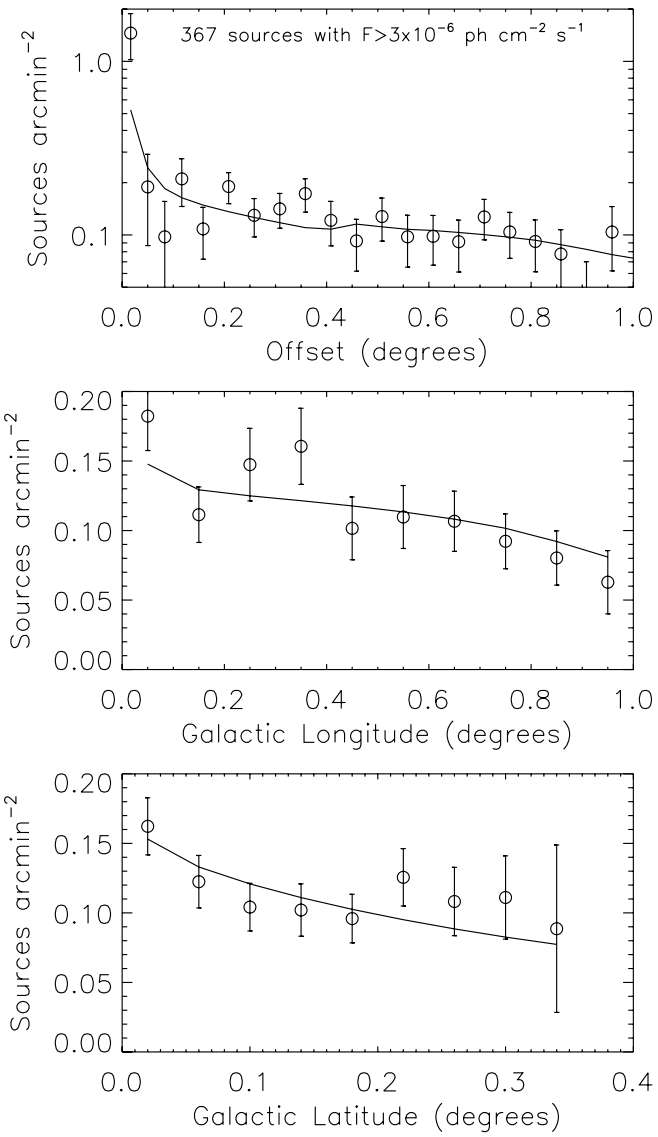

FIG. 4.—Distributions of point sources as a function of angular offset from Sgr A* (*top panel*), and the absolute values of Galactic longitude (*middle panel*) and latitude (*bottom panel*). We only considered sources that were brighter than $F_{\rm X} = 3 \times 10^{-6}$ photons cm^{-2} s^{-1}, that had a 50% chance of being detected, and that lay in regions where the 50% detection threshold was lower than the above flux limit. The contribution of each source to the distribution was weighted by the inverse of the probability of detecting it. The surface density of stellar mass is plotted with the solid line, which has been normalized through a χ^2 minimization to match the surface density of X-ray sources. In all cases, the normalization implied that there were 4×10^{-7} X-ray sources with $F_{\rm X} \geq 3 \times 10^{-6}$ photons cm^{-2} s^{-1} for every 1 $M_\odot$ of stars.

We model the Galactic bulge as a triaxial ellipsoid of the form

$$\rho = \rho_{\rm bulge} e^{-r_s}, \tag{3}$$

$$r_s = \left[(r_\perp)^{c_\parallel} + \left(\frac{|x|}{a_x} \right)^{c_\parallel} \right]^{1/c_\parallel}, \tag{4}$$

$$r_\perp = \left[\left(\frac{|x|}{a_x} \right)^{c_\perp} + \left(\frac{|y|}{a_y} \right)^{c_\perp} \right]^{1/c_\perp}. \tag{5}$$

The axis defining x, y, z is rotated 15° east and 1° north from our line of sight. The parameters are $a_x = 1100$ pc, $a_y = 360$ pc,

TABLE 3
PARAMETERS OF THE $\log N - \log S$ DISTRIBUTION

Field	$S_{\rm lim}$ (10^{-6} photons cm^{-2} s^{-1})	Number of Sources	Area (arcmin^2)	α	N_0 (arcmin^{-2})	$P_{\rm KS}$
Sgr B2	0.6	48	95	1.6 ± 0.2	0.04	0.99
Radio arches	2	27	97	1.1 ± 0.2	0.16	0.69
Shallow survey	6	144	2834	1.3 ± 0.1	0.10	0.34
Sgr A*	0.8	232	152	1.4 ± 0.1	0.21	0.01

NOTES.—The normalization of the $\log N - \log S$ distribution, N_0, is listed for a fiducial flux of 3×10^{-6} photons cm^{-2} s^{-1}, to match the spatial distribution in Fig. 4. $P_{\rm KS}$ represents the probability under a K-S test of seeing the observed difference between the observed and model distribution assuming that they are identical, so that very small values would indicate a poorer match.

$a_z = 220$ pc, $c_\perp = 1.6$, $c_\parallel = 3.2$, and $\rho_{\rm bulge} = 8\ M_\odot\ {\rm pc}^{-3}$. The total mass of the bulge is taken to be $10^{10}\ M_\odot$.

Finally, we model the Galactic disk as a simple exponential,

$$\rho = \rho_0 \exp(-r/r_d) \exp(-|z|/z_d), \quad (6)$$

where $r_d = 2.7$ kpc, $z_d = 200$ pc, and $\rho_0 = 5\ M_\odot\ {\rm pc}^{-3}$, so that the total mass of the disk is $10^{11}\ M_\odot$.

We integrated the model stellar density along our line of sight toward the Galactic center, using a lower limit of 6 kpc because we excluded foreground sources from the profiles in Figure 4 and an upper limit of 10 kpc because sources beyond this distance will be heavily absorbed and difficult to detect. We then compared these model surface densities to the observed surface density of X-ray sources through a linear χ^2 minimization. We did not attempt to correct the surface density of X-ray sources to account for fact that the absorption column varies as a function of longitude, latitude, and along our line of sight in the image, because the uncertainty introduced by our failure to do so is smaller than the $\approx$50% uncertainty in the mass model. The best-fit stellar surface densities are indicated by solid lines in Figure 4. The overall match is good, with $\chi^2/\nu < 1$. However, within 2′ of Sgr A* (4.7 pc in projection) the number of X-ray sources is 2 σ larger than that expected from a simple scaling of the mass distribution inferred from the infrared (1.3 ± 0.4 sources arcmin^{-2} vs. the predicted 0.5 sources arcmin^{-2}). This may be further evidence that X-ray sources are more concentrated near Sgr A* than ordinary stars are (see also Muno et al. 2005). The normalization of the fits imply that above a limit of 5×10^{32} ergs s^{-1} there are $(4 \pm 2) \times 10^{-7}$ X-ray sources per solar mass of stars, where most of the uncertainty is in the mass models. We compare this to the expected density of X-ray sources in § 4.

3.2. *Number-Flux Distribution*

Spatial variations in the underlying population of X-ray sources could be identified by examining the relative number of faint and bright X-ray sources. Therefore, we have computed the cumulative $\log N - \log S$ distributions in four regions: the Arches field, the Sgr B2 field, the general shallow survey (excluding the deep pointings), and the Sgr A* field (see also Muno et al. 2003). However, in this case, we required that each source had at least a 90% chance of being detected, which was stricter than when we studied the spatial distribution. We modeled the differential number-flux distribution using the method described in Murdoch et al. (1973), with slight modifications described in Appendix B to use Poisson statistics and knowledge of the average background rate. As for the spatial distribution, we defined a flux limit ($S_{\rm lim}$) for each region above which we could securely detect sources over the largest possible area. For the $\log N - \log S$ distribution, we added the criterion that the flux limit allow us to measure the fluxes of sources at the 5 σ level. Our choice of flux limits is described in more detail in Appendix B. The flux limits, area covered by each survey, and number of sources that were brighter than $S_{\rm lim}$ and located at points where sources with $S = S_{\rm lim}$ could be detected securely are listed in Table 3.

In Table 3, we also list the best-fit slopes α, the normalizations N_0 at $S_0 = 3 \times 10^{-6}$ photons cm^{-2} s^{-1} (the fit had to be extrapolated for the shallow survey because the faintest securely detected sources had $S = 6 \times 10^{-6}$ photons cm^{-2} s^{-1}), and the probabilities $P_{\rm KS}$ that the model and observed distributions match according to the Kolmogorov-Smirnov (K-S) test. All of the models, except that for Sgr A*, are consistent with the data within the uncertainties provided by our limited numbers of sources, as indicated by the large values of the chance probability ($P_{\rm KS} \gtrsim 0.1$). The increase in the normalization of the distributions is consistent with the radial distribution of point sources in Figure 4. We find marginal, 1 σ evidence that the $\log N - \log S$ distribution is flatter in the Radio Arches region than in the Sgr B2 field or the survey as a whole, which would imply that the former contains a larger proportion of high-luminosity sources. Unfortunately, our constraints on the $\log N - \log S$ distribution are a bit poor, because the number of sources that meet the criterion of having >5 σ flux measurements (roughly, >25 photons) is small (see Fig. 2). The best-fit distributions are plotted with solid lines in Figure 5.

In Figure 5, we also plot the expected distributions of background active galactic nuclei (AGNs). To convert between the photon fluxes we use here and the 2–8 keV energy flux that is reported in papers on the *Chandra* and *XMM-Newton* deep fields, we assume that AGNs are observed through an absorption column of 12×10^{22} cm^{-2} and that their spectra are described by a $\Gamma = 1.5$ power law (the final results are not sensitive to a choice of Γ between 1.2 and 1.8). We find that a source with a 0.5–8.0 keV photon flux of $S_0 = 3 \times 10^{-6}$ photons cm^{-2} s^{-1} in our survey would have a 2–8 keV flux of 6×10^{-14} ergs cm^{-2} s^{-1} if it were located at high Galactic latitude. Only a couple of sources this bright are detected in a typical extragalactic field (e.g., Brandt et al. 2001). From Manners et al. (2003), the $\log N - \log S$ distribution of X-ray sources with fluxes of $(0.1-5) \times 10^{-6}$ photons cm^{-2} s^{-1} [$(0.02-1) \times 10^{-13}$ ergs cm^{-2} s^{-1}] has a slope of $\alpha = 1.07$ and a normalization of 0.008 sources arcmin^{-2} at a flux of 3×10^{-6} photons cm^{-2} s^{-1}. This normalization is <10% of that of the shallow survey in Table 3 (see also Fig. 4). Above 1×10^{-13} ergs cm^{-2} s^{-1}, Ueda et al. (1999) find that the cumulative distribution steepens to $\alpha = 1.5$, with a normalization of 0.004 sources arcmin^{-2} at 5×10^{-6} photons cm^{-2} s^{-1} (1×10^{-13} ergs cm^{-2} s^{-1}). Cosmic variance could change the extragalactic source contribution by no more than $\approx$50% (e.g., Manners

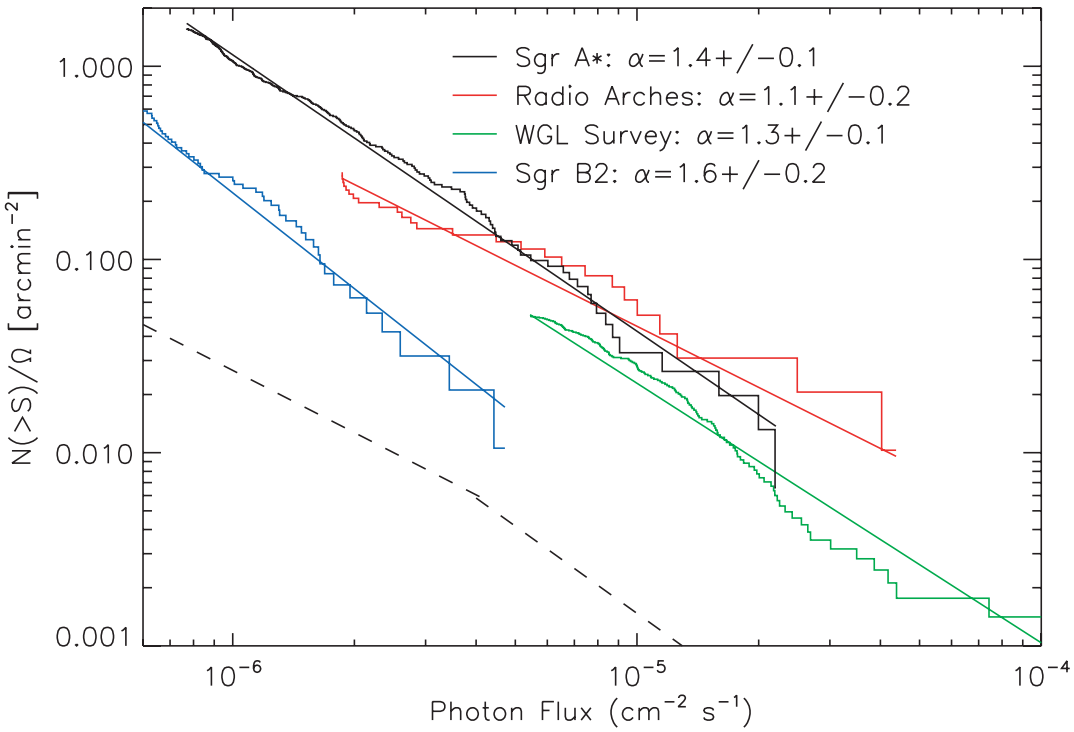

FIG. 5.—Number-flux distribution of sources in the Arches region (*red lines*), the Sgr B2 region (*blue lines*), and the shallow survey (*green lines*). The solid histograms have been corrected for the detection probability and are only plotted for sources brighter than the flux limits used in modeling the distributions. The solid lines are the best-fit model distributions [$N(>S) \propto S^{-\alpha}$], with the slopes indicated in the top right of the figure. Most of the power-law fits are consistent with the data, given the relatively small numbers of sources in the distributions. The fit to Sgr A* is inconsistent with the data but is included for comparison purposes; see Muno et al. (2003) for a more complete discussion. The dashed lines represent the background AGN contributions taken from Manners et al. (2003) ($<4 \times 10^{-6}$ photons cm^{-2} s^{-1}) and Ueda et al. (1999) ($>4 \times 10^{-6}$ photons cm^{-2} s^{-1}).

et al. 2003; Bauer et al. 2004). Therefore, $\lesssim$130 of the absorbed sources in our sample should be extragalactic.

4. DISCUSSION

We have presented a catalog of X-ray sources with fluxes between a few times 10^{31} and 10^{35} ergs s^{-1}. The majority of the region was covered with tiled pairs of 12 ks observations, in which the 50% completeness limit is 1×10^{33} ergs s^{-1}. Two deeper exposures were more sensitive. A 50 ks observation toward the Radio Arches was complete to 4×10^{32} ergs s^{-1}, and a 100 ks observation toward Sgr B2 was complete to 1×10^{32} ergs s^{-1}. The sensitivity of the Radio Arches observation was a factor of 2 poorer than would be naively expected based on the exposure time, because the Galactic center produces strong diffuse emission against which point sources are more difficult to detect.

Our survey encompasses a nontrivial fraction of the mass of stars in the Galaxy. Integrating the Launhardt et al. (2002) models for the stellar distribution over our survey area, we find that it encloses a stellar mass of $\sim 10^9\ M_\odot$, or 1% of the Galactic value. In Table 4, we list the various classes of object that could be detected as X-ray sources in our image if they were located near the Galactic center. We also include predictions for the total number of each class of sources encompassed by the survey region. For the most part, we scale the Galactic population down to that at the Galactic center by assuming that the star formation rate is $\sim$1% of the Galactic value, or 0.01 $M_\odot$ yr^{-1} (Figer et al. 2004). However, if the recent rate of star formation in the central 150 pc of the Galaxy is $\sim$10% of the total Galactic rate, as is suggested by indirect measurements of the Lyα flux in the region (Cox & Laureijs 1989; Figer et al. 1999), then WR/O stars, luminous pulsars, and high-mass X-ray binaries each could be an order of magnitude more numerous. Below we describe the considerations that went into developing that table, and some implications that the observed population of sources have for understanding the evolution of the accreting binaries that make up the majority of our sample.

4.1. *Comparison to the Local Galactic X-Ray Population*

We start by comparing the amount of X-ray flux per unit stellar mass from the point sources with $L_X > 5 \times 10^{32}$ ergs s^{-1} in our survey to that in the local Galaxy as identified by Sazonov et al. (2006). For a cumulative number-flux distribution of the

TABLE 4
X-RAY SOURCES IN THE GALACTIC CENTER

Object	log (L_X) [log (ergs s^{-1})]	Number in GC	Number Detectable	References
CVs	29.5–33.5	10^5	10^3	1, 2
WR/O stars	31–34	10^3	10	3, 4, 5
Pulsars	29.3–35	10^6	10	6, 7
LMXBs	30–39	10^3	10	8, 9, 10
HMXBs	31–38	10^3	50	11

NOTE.—We list order-of-magnitude estimates of the total population of various X-ray sources in our field, along with the number that should be detected in our survey (see text).

REFERENCES.—(1) Verbunt et al. 1997; (2) Sazonov et al. 2006; (3) Figer et al. 2004; (4) Pollock 1987; (5) Berghöfer et al. 1997; (6) Becker & Aschenbach 2002; (7) Cordes & Lazio 1997; (8) Wijnands et al. 2002a; (9) Liu & Li 2006; (10) Kong et al. 2002; (11) Pfahl et al. 2002.

form $N(>L_X) = N_0(L_X/L_{X,0})^{-\alpha}$, the specific luminosity produced by sources with $L_{X,\min} < L_X < L_{X,\max}$ is

$$\mathcal{L}_{X,\rm tot} = \frac{\alpha N_0 L_{X,0}}{\alpha - 1}\left[\left(\frac{L_{X,\min}}{L_{X,0}}\right)^{-\alpha+1} - \left(\frac{L_{X,\max}}{L_{X,0}}\right)^{-\alpha+1}\right], \quad (7)$$

where N_0 is the normalization at a luminosity of $L_{X,0}$ in units of sources per solar mass. For the Galactic center, from the $\log N - \log S$ function we have found that $\alpha = 1.5$ (Table 3, Fig. 4), and from the spatial distribution we have found that $N_0 = (4 \pm 2) \times 10^{-7}$ sources $M_\odot{}^{-1}$ at $L_{X,0} = 5 \times 10^{32}$ ergs s^{-1} (§ 3.1). So, the specific luminosity of X-ray point sources with luminosities between $L_{X,\min} = 5 \times 10^{32}$ ergs s^{-1} and $L_{X,\max} = 10^{34}$ ergs s^{-1} in our survey is $\mathcal{L}_{X,\rm tot} = (5 \pm 2) \times 10^{26}$ ergs s^{-1} $M_\odot{}^{-1}$. In the local Galaxy, Sazonov et al. (2006) find that $\alpha \approx 1.2$ and $N_0 = (6 \pm 2) \times 10^{-4}$ sources $M_\odot{}^{-1}$ at $L_{X,0} = 2 \times 10^{30}$ ergs s^{-1} (where for K in their eq. [5], $N_0 = K/\alpha$, and we have estimated the uncertainty based on that of total specific luminosity for sources with $L_X < 10^{34}$ ergs s^{-1}). So, the specific luminosity of sources with luminosities between $L_{X,\min} = 5 \times 10^{32}$ ergs s^{-1} and $L_{X,\max} = 10^{34}$ ergs s^{-1} is locally $\mathcal{L}_{X,\rm tot} = (1.0 \pm 0.3) \times 10^{27}$ ergs s^{-1} $M_\odot{}^{-1}$. Therefore, the specific luminosities of X-ray sources with 5×10^{32} ergs s^{-1} $< L_X < 10^{34}$ ergs s^{-1} in the local Galaxy and in the Galactic center are consistent within their uncertainties.

To understand the population of X-ray sources at the Galactic center, it is notable that in the local Galactic neighborhood all the X-ray sources with 10^{32} ergs s^{-1} $< L_X < 10^{34}$ ergs s^{-1} (2–10 keV) are cataclysmic variables (CVs) with magnetic white dwarfs and orbital periods of several hours (intermediate polars; Sazonov et al. 2006). Therefore, it is conceivable that most of the X-ray sources with $L_X < 10^{34}$ ergs s^{-1} in our survey are magnetic CVs (see also Muno et al. 2004; Laycock et al. 2005). We would expect CVs to have the same spatial distribution as the old ($\gtrsim$Gyr) population of stars, which dominate the infrared light from the Galaxy, and indeed the distribution of X-ray sources is identical to the inferred distribution of stars (Fig. 4). As described in Muno et al. (2004), intermediate polars have particularly hard, intrinsically absorbed spectra that are consistent with those of the sources with $L_X \lesssim 10^{33}$ ergs s^{-1} in Figure 3.

Few CVs have $L_X > 10^{33}$, and only one CV has been observed at $L_X \gtrsim 5 \times 10^{33}$ ergs s^{-1} (GK Per in outburst; e.g., King et al. 1979), so we expect brighter sources to be more luminous objects such as LMXBs, HMXBs, WR/O stars in colliding-wind binaries, or pulsars (Table 4). The excess of bright X-ray sources observed in the Radio Arches field (Fig. 5), in which the Arches and Quintuplet clusters are striking evidence of recent active star formation (Figer et al. 1999), can be explained if some of the bright sources are HMXBs, WR/O stars, or young pulsars. Such sources have short lifetimes and so should be concentrated near regions of active star formation. Such sources also have softer spectra than intermediate polars in the 2–8 keV band and so could explain why the sources brighter than $\sim 10^{33}$ ergs s^{-1} in Figure 3 are systematically softer than the faint ones.

4.2. *Comparison to Theoretical Models*

Several binary population synthesis calculations have been carried out in order to interpret the population of X-ray sources in the Galactic center described by Wang et al. (2002) and Muno et al. (2003). These models outline how the numbers of each class of X-ray sources constrain various combinations of parameters in the binary evolution models and assumptions about the physics of systems accreting at low rates.

For instance, Pfahl et al. (2002) suggested that several hundred of the X-ray sources in the Wang et al. (2002) survey could be neutron stars accreting from the winds of >3 $M_\odot$ binary companions (see also Belczynski & Taam 2004). The total numbers of wind-accreting neutron stars, and the fractions of systems with companions more and less massive than 8 $M_\odot$, vary by a factor of a few depending on the magnitudes of the kicks imparted to the neutron stars at birth. These theoretical predictions have motivated searches for infrared counterparts to the X-ray sources in the Galactic center surveys (Laycock et al. 2005; Bandyopadhyay et al. 2005). However, Liu & Li (2006) suggested that accretion could be inhibited by the magnetospheres of the neutron stars (see also Davies & Pringle 1981) at the low mass-transfer rates considered by Pfahl et al. (2002), so that wind-accreting neutron stars may not be luminous enough to be detected in our *Chandra* survey. For Table 4, we assume that they will be detectable, but we use the most conservative estimates of their numbers from Pfahl et al. (2002).

There also is theoretical disagreement as to whether CVs contribute significantly to the population of X-ray sources in our survey. Liu & Li (2006), who base their calculations on the binary evolution code of Hurley et al. (2002), suggest that CVs are not luminous enough to be detected in large numbers from the Galactic center. However, this disagrees with similar calculations by Ruiter et al. (2006), who use the StarTrack code (Belczynski et al. 2005) and predict that significant numbers of luminous CVs should be detectable from the Galactic center. The main difference between the two codes is in their prescriptions for calculating the rate of mass transfer, which leads Liu & Li (2006) to predict mass transfer rates $\sim$100 times lower than those used by Ruiter et al. (2006) for identical systems with orbital periods of several hours (A. Ruiter 2005, private communication). Systems with orbits of several hours have the highest accretion rates (Patterson 1984; see also Howell et al. 2001) and therefore are the most luminous in X-rays, which makes them the most important contributors among CVs to our survey. Our comparison with the local Galactic population of X-ray sources suggests that CVs are indeed both numerous and luminous enough to explain the population of X-ray sources in our image (see also, e.g., Verbunt et al. 1997; Ezuka & Ishida 1999; Suleimanov et al. 2005), so our results could be taken as further, indirect evidence in support of the prescription used by Belczynski et al. (2005) and Ruiter et al. (2006). In Table 4, we assume that the number of CVs in the Galactic center can be scaled by mass from the local Galactic population, which is consistent with the calculations of Ruiter et al. (2006).

Finally, Belczynski & Taam (2004) and Liu & Li (2006) predict that there are a few thousands LMXBs consisting of a neutron star accreting from a white dwarf in our survey region. In these models, most of the neutron stars in these systems form through the accretion-induced collapse of an ONe white dwarf. Under the assumptions of Liu & Li (2006), a few percent of the LMXBs are persistently bright enough to be detected in our survey. Moreover, most of these LMXBs should be transient, so if one assumes a standard duty cycle of $\sim$1%, there should be >50 LMXBs in outburst with $L_X > 10^{36}$ ergs s^{-1} in the field at any given time (and thousands in the Galaxy). In contrast, there are only two persistent LMXBs this luminous in the field, 1E 1743.1−2843 and 1E 1740.7−2942 (Wang et al. 2002), and several decades of occasional X-ray observations have revealed only about a dozen transients with $L_X \gtrsim 10^{36}$ ergs s^{-1} (and only $\sim$150 in the rest of the Galaxy; see, e.g., Liu et al. 2001; Wijnands et al. 2006). The production of a large number of these transient LMXBs appears to be a common feature of models in which neutron stars can

form through accretion-induced collapse (e.g., § 5.6 of Iben et al. 1995). Under the models of Belczynski & Taam (2004) and Liu & Li (2006), possible ways to accommodate the small number of bright transients in our field are to assume that the efficiency with which the envelope of a star can be ejected during the common envelope phase is low so that many of the binaries merge rather than forming LMXBs, or to assume that the accretion-induced collapse of an ONe white dwarf does not form a neutron star. In Table 4, we use the numbers of persistent LMXBs in Belczynski & Taam (2004) and Liu & Li (2006), but ignore the predicted number of bright transients because they are clearly not detected in our observations.

5. THE FUTURE

Further progress in understanding the natures of the X-ray sources near the Galactic center, and the consequential constraints on the parameters input into binary evolution and population synthesis models, will be acquired through multiwavelength observations of the region. X-ray observations will add to the population of transient LMXBs in the field (e.g., Wang et al. 2002; Sakano et al. 2005; Muno et al. 2005; Wijnands et al. 2006). Comparing infrared and X-ray surveys will reveal individual examples of WR/O binaries and HMXBs (e.g., Bandyopadhyay et al. 2005; Muno et al. 2006). The first pulsars near the Galactic center may be found by comparing radio and X-ray surveys (see also Cordes & Lazio 1997).

This catalog will be improved on greatly in the next year. First, these fields are being analyzed as part of the ChaMPlane survey (Grindlay et al. 2005), and so the spatial distributions and $\log N - \log S$ functions will be compared with those in the Galactic disk and old portions of the Bulge (Hong et al. 2005a). Moreover, series of deep, 40 ks exposures of roughly half of the survey area have been approved for the 2006 *Chandra* observing cycle. We expect to increase the number of X-ray sources detected by a factor of ≈ 5 and improve the uncertainties on the positions of the sources in the shallow survey from $\approx 1''$ to $< 0''.5$. In the meantime, the current catalog provides the best available sample for studying the spatial and number-flux distributions of X-ray sources near the Galactic center and for identifying their counterparts at other wavelengths.

We thank the referee, S. Laycock, for helpful comments on the manuscript and data analysis, M. Morris for advice about the project, K. Belczynski for discussions about population synthesis models, and especially A. J. Ruiter and X. Liu for performing calculations to help clarify the differences between various population synthesis codes. M. P. M. and F. E. B. acknowledge support from NASA/SAO under grant AR5-6018A, and Q. D. W. acknowledges support from NASA/SAO under grant GO4-5010X. M. P. M. also was supported under a Hubble Fellowship, and FEB under a Chandra Fellowship.

APPENDIX A

COMPLETENESS OF THE SURVEY

In order to study the spatial and luminosity distributions of the X-ray sources, we need to calculate the limiting flux at which we can confidently detect sources as a function of position in the survey. We performed synthetic star tests following the basic method of Bauer et al. (2004), with modifications to account for differences in our treatment of the photometry and the more complex layout of our survey.

In order to produce $\sim 10^5$ synthetic stars, we simulated 1000 exposures of ObsID 2287 (12 ks exposure), and 100 each for ObsIDs 945 (50 ks exposure) and 944 (100 ks exposure). For each observation, we removed events from within a circle circumscribing 92% of the energy of the PSF around each detected source. We then created images from the resulting event lists and filled the "holes" in the image with a number of counts drawn from a Poisson distribution with a mean equal to that of a surrounding annulus. Each point source was assigned to a random position in the image. We drew fluxes for synthetic stars from a power-law distribution $N(>S) \propto S^{-\alpha}$ with a slope $\alpha = 1.5$, normalizations and flux limits chosen to match the numbers and intensities of sources in each region (e.g., Table 3). We converted these fluxes to count rates using an exposure map generated for photons with $E = 3$ keV and then drew net numbers of counts from Poisson distributions with those mean count rates. Next, we obtained a model image of the PSF created by `mkpsf` when computing the photometry for the nearest detected source in the image and used the PSF as the probability distribution to simulate the two-dimensional image of the counts. In most cases, the model PSF was from a source located well within $1'$ of the simulated star, and the offset was never larger than $2'$. The simulated source was then placed into the composite image. Finally, we searched the synthetic image for point sources using `wavdetect` and tabulated which sources we placed into the image were detected by our search algorithm.

We display the fraction of sources that are detected in 12, 50, and 100 ks as a function of input flux and offset from the aim point in Figure 6. The probability of detecting a source obviously increases with larger flux, because there is a higher signal-to-noise ratio. For a given flux, the probability of detecting a source is also larger at small offsets from the aim point, because farther from the aim point counts are spread over a larger area by the PSF. This latter trend can also be seen in Figure 7, where we have plotted the number of counts above which a source will be detected 50% and 90% of the time as a function of offset from the aim point. As expected, longer observations enable us to reliably detect sources with lower fluxes. However, the total background counts from diffuse X-ray emission toward the Galactic center also increases for longer exposures, so more counts are required to reliably detect a source. As a result, a factor of 5 increase in exposure from 10 to 50 ks yields only a factor of 3 increase in sensitivity, which is by no means linear, but it is still a faster improvement than the $t^{-1/2}$ trend that would be expected if we were background-limited.

We used the above simulations to make a map of the sensitivity of our survey. For each observation, we generated a sensitivity map by (1) computing the offset of each pixel from the aim point, (2) computing the count threshold from Figure 7, and (3) dividing the count threshold by the exposure map (in units of cm^2 s) to obtain a flux. Then, to create a composite map for the full survey, for each pixel we recorded the lowest value of the flux threshold from all of the maps with exposure at that pixel. We note that using this method, localized enhancements in the diffuse emission that decrease our sensitivity have been averaged over offset from the aim point. Properly accounting for all of the variations in the diffuse emission would require that we carry out our Monte Carlo simulations

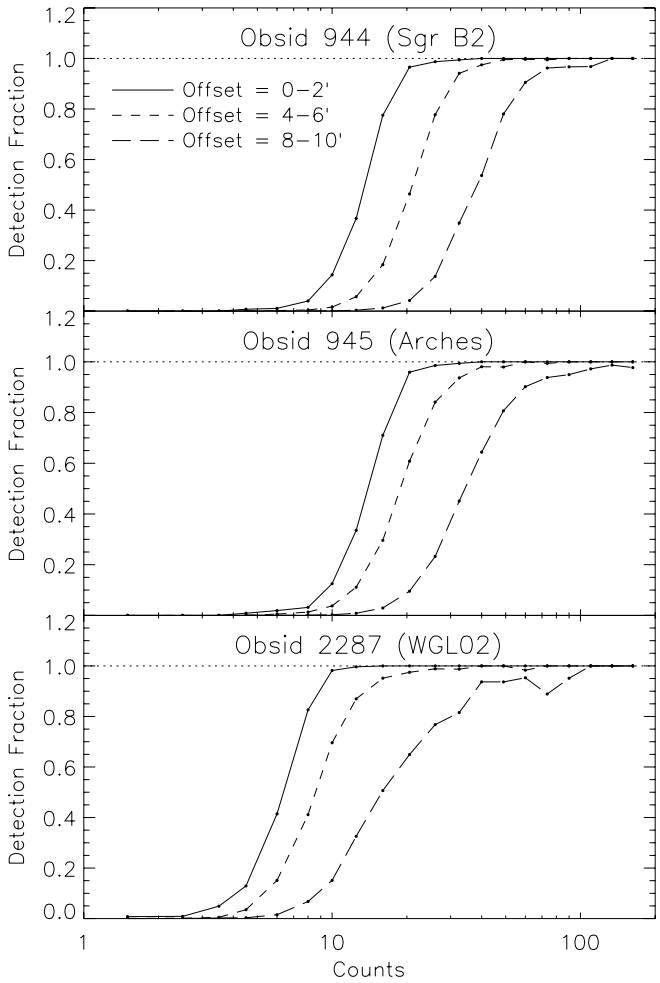

FIG. 6.—Probability of detecting a source as a function of count rate (y-axis) and offset (*line styles*). The detection probability depends on the survey region because of variations in the diffuse X-ray background; the longer observations are background-limited. The probability at a given count rate decreases as the offset increases, because the size of the PSF increases. We note that the curve for the 8′–10′ offset in the shallow (WGL02) survey was not used much, because sources in that survey almost always were found closer to the aim point of at least one of the tiled pointings.

for each exposure, which would be time-consuming and would not change our results significantly. The resulting map is displayed in Figure 8. We also have tabulated the area over which our survey is sensitive as a function of limiting flux, and displayed that in Figure 9.

We have also used the simulations to compute the probability of detecting each source. For each source, we determined the offset from the aim point of the most sensitive exposure, and determined the count threshold at that offset from Figure 7. We then divided that count threshold by the exposure map from the most sensitive observation at the location of the source to obtain a flux threshold. Again, this technique ignores local background variations that introduce systematic errors in our computed thresholds for individual sources, but these errors should average out when considering large numbers of sources. The median probability of detecting a Galactic center source was 57%. This is because the photons from faint sources are often lost to the wings of the PSF, and because the number-flux distribution is quite steep (see § 3.2), so many faint sources are only detectable when Poisson fluctuations result in larger observed counts (this produces the Eddington bias when computing number-flux distribution).

The sensitivity maps and detection probabilities were used in computing the spatial distribution in § 3.1 and flux distributions in § 3.2. We also repeated the above process for the combined image created from 625 ks of exposure on the $17' \times 17'$ field around Sgr A*, so that we could compare the results from the catalog in Muno et al. (2003) to the current one. We find that a source can be detected confidently with the fewest counts in the shallow survey (Fig. 7), because the longer observations were background-limited. Of course, the observations were still more sensitive when the detection threshold was considered as a function of flux (Fig. 9).

APPENDIX B

MODELING THE NUMBER-FLUX DISTRIBUTION

We modeled the unbinned number-flux distributions using the technique described in Murdoch et al. (1973). We assumed that the cumulative number-flux distribution could be described as a power law $N(>S) \propto S^{-\alpha}$, where S is the net number of counts for a source, and that the number of observed counts could be described by a Poisson distribution with mean rate $S + B$, where B is the

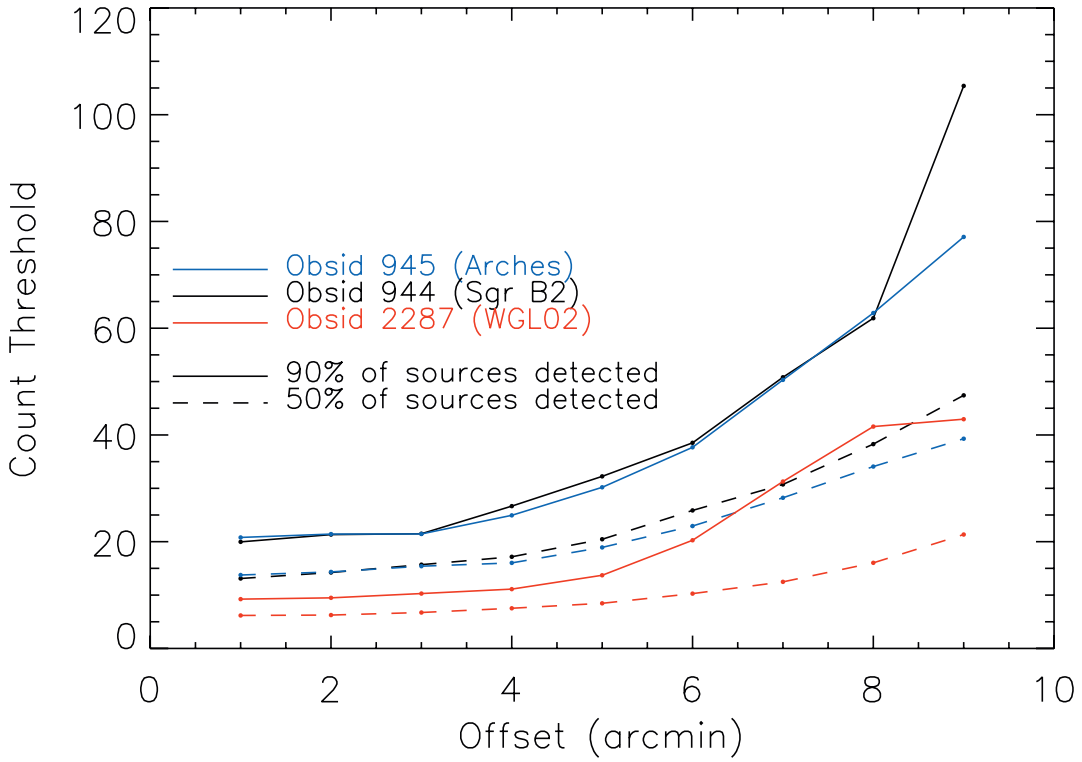

FIG. 7.—Number of counts required to detect a source in 50% (*dashed line*) and 90% (*solid line*) of trials, as a function of offset from the center of the cluster. In order of decreasing number of counts required, the red line is for the Arches region, the blue line for Sgr B2, and the green line for the shallow survey.

average number of background counts in the source extraction region (e.g., $B = 4.3$ for the shallow survey). The likelihood of observing sources with a distribution of total counts C_i (which are all integers) is then

$$\sum_i \ln P(C_i) = \sum_i P_{\mathrm{det},i} K^{-1} \int_0^\infty \frac{e^{-(S+B)}(S+B)^{C_i}}{C_i!} N_0 S^{-(\alpha+1)}\, dS, \tag{B1}$$

where K is normalization over the range of count rates under consideration (C_l, C_u),

$$K = \int_0^\infty \sum_{C_l}^{C_u} P_{\mathrm{det},i} \frac{e^{-(S+B)}(S+B)^{C_i}}{C_i!} N_0 S^{-(\alpha+1)}\, dS. \tag{B2}$$

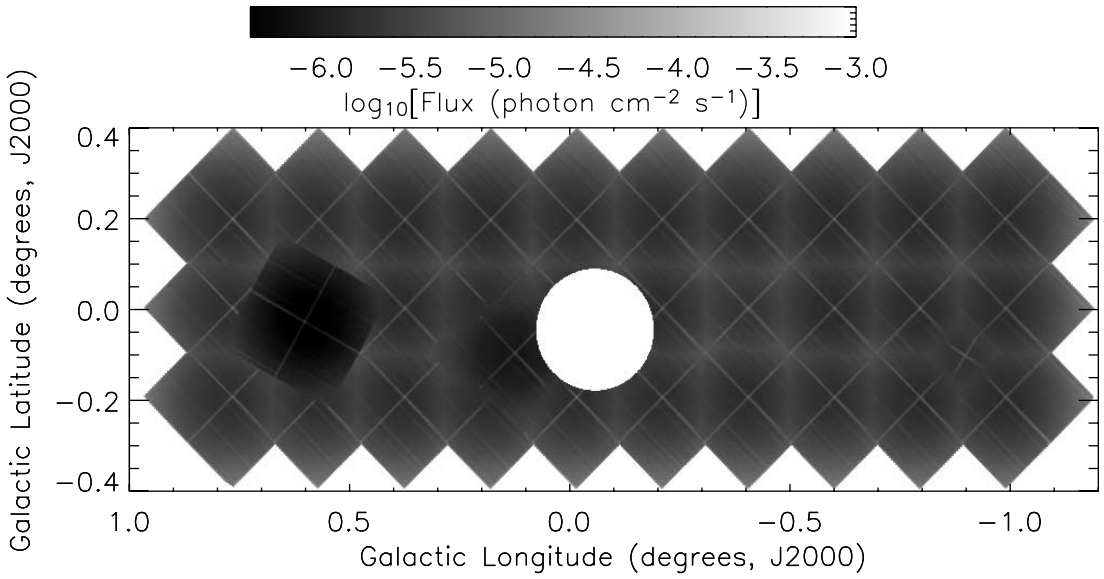

FIG. 8.—Map of the 50% detection threshold over our survey. The large white circle at the center represents the region covered by the deep survey in Muno et al. (2003). We do not include sources in that region in our catalog.

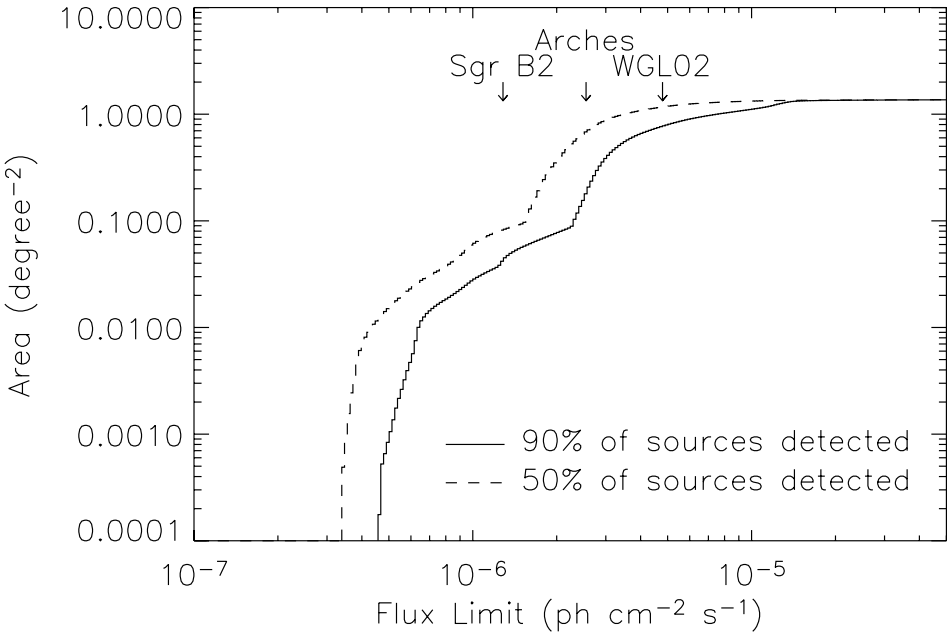

FIG. 9.—Area over which we were sensitive to sources of given fluxes. The mean sensitivity of the Sgr B2, Arches region, and shallow surveys are indicated with arrows.

The normalization of the power law N_0 drops out of equation (B1), and so it was derived by setting the normalization K for the best-fit α equal to the observed number of sources. Finally, we compared the observed cumulative flux distribution to the model distribution P_i using a K-S test, to establish whether our power-law model is consistent with the data.

Caution needs to be used in exercising these equations, as is described in detail in Murdoch et al. (1973). First, the integrals over S will diverge as S approaches 0 unless a the count rate from a source is inconsistent with the background rate B at the $\approx 5\ \sigma$ level (Murdoch et al. 1973; Wang 2004). Therefore, we restricted our analysis to sources brighter than the 5 σ detection threshold for the average background level in each region. The mean background and count thresholds are listed in Table 3. In doing so, we were able to ignore the negligible contributions to the above integrals from beyond $S \approx (C_i) \pm 12(C_i)^{1/2}$. Second, our source-detection algorithm was designed primarily to reject false positives, and we find that false negatives occur for $\approx$20% of sources with count rates at the 5 σ level above background (we ascribe the high false-negative rate to the fact that the uncertainty in our flux calculation only depends on the number of counts, whereas the detection algorithm depends both on the number and the spatial distribution of the counts). We use the factor $P_{\mathrm{det},i}$ in the above equations to account for the probability of detecting a source with a count rate C_i, which we determined from our Monte Carlo simulations. Third, in order to avoid being biased by bright sources detected in regions with poor sensitivity, we only considered regions of the image in which there was a >90% chance of identifying a source with a flux equal to the 5 σ detection threshold. We list in Table 3 the number of sources that met these criteria and the area over which we were sensitive. Finally, we note that we used average values for the background and the detection probability, even though both varied significantly over the regions covered by each set of observations. The total counts C_i used above were the sum of the net counts derived from our photometry and the average background, which was then rounded to the nearest integer. This was necessary to ensure that the integrand in equations (B1) and (B2) were monotonic functions of C_i (see also Wang 2004).

Our approach to modeling the $\log N - \log S$ distribution takes into account the possible Eddington bias, although it ignores the vast majority of faint sources. Different approaches are possible and should yield similar results. For instance, Bauer et al. (2004) used Monte Carlo simulations to estimate the corrections to the flux required to offset both the Eddington bias and biases introduced by their method for deriving the photometry for each source, assumed that the photometric uncertainties were negligible, and analytically computed α from a maximum-likelihood distribution using corrected fluxes and the equations in Murdoch et al. (1973). We have not implemented this technique, because our procedure for computing the photometry for each source was computationally prohibitive to incorporate it into our Monte Carlo simulations. We also note that their resulting slope could be somewhat biased, because they have assumed a $\log N - \log S$ distribution in computing the flux correction, thereby predetermining the effect of the Eddington bias.

Wang (2004) has presented a method that is almost equivalent to ours, in which he applied a redistribution matrix to convert a model distribution into an observed distribution and then found best-fit parameters for the model using the χ^2 and Cash minimization techniques implemented in XSPEC (Arnaud 1996). If the model and unbinned fluxes are compared using the Cash statistic (Cash 1979), the techniques are equivalent, although the use of a response matrix converts the integral in equation (B1) into a sum. Using binned data and a χ^2 test obviously requires enough sources per bin that their numbers are approximately distributed as a Gaussian. That technique has the advantage of using tools that X-ray astronomers are familiar with, although it is conceptually more complicated than our method.

REFERENCES

Arnaud, K. A. 1996, in ASP Conf. Ser. 101, Astronomical Data Analysis Software and Systems V, ed. G. Jacoby & J. Barnes (San Francisco: ASP), 17
Baganoff, F. K., et al. 2003, ApJ, 591, 891
Bandyopadhyay, R. M., et al. 2005, MNRAS, 364, 1195
Bauer, F. E., Alexander, D. M., Brandt, W. N., Schneider, D. P., Treister, E., Hornschmeier, A. E., & Garmire, G. P. 2004, AJ, 128, 2048
Becker, W., & Aschenbach, B. 2002, in Neutron Stars, Pulsars, and Supernova Remnants, ed. W. Becker, H. Lesch, & J. Trümper (MPE Rep. 278; Garching: MPE), 64
Belczynski, K., Kalogera, V., Rasio, F. A., Taam, R. E., Zezas, A., Bulik, T., Maccarone, T. J., & Ivanova, N. 2005, ApJS, submitted (astro-ph/0511811)
Belczynski, K., & Taam, R. E. 2004, ApJ, 616, 1159
Berghöfer, T. W., Schmitt, J. H. M. M., Danner, R., & Cassinelli, J. P. 1997, A&A, 322, 167
Brandt, W. N., et al. 2001, AJ, 122, 2810
Cash, W. 1979, ApJ, 228, 939
Cordes, J. M., & Lazio, T. J. W. 1997, ApJ, 475, 557
Cox, P., & Laureijs, R. 1989, in IAU Symp. 136, The Center of the Galaxy, ed. M. Morris (Dordrecht: Kluwer), 121
Davies, R. E., & Pringle, J. E. 1981, MNRAS, 196, 209
de Pree, C. G., Goss, W. M., & Gaume, R. A. 1998, ApJ, 500, 847
Ezuka, H., & Ishida, M. 1999, ApJS, 120, 277
Figer, D. F., Kim, S. S., Morris, M., Serabyn, E., Rich, R. M., & McLean, I. S. 1999, ApJ, 525, 750
Figer, D. F., Rich, M. R., Kim, S. S., Morris, M., & Serabyn, E. 2004, ApJ, 601, 319
Freeman, P. E., Kashyap, V., Rosner, R., & Lamb, D. Q. 2002, ApJS, 138, 185
Grindlay, J. E., Hong, J., Zhao, P., Laycock, S., van den Berg, M., Koenig, X., & Schlegel, E. M. 2005, ApJ, 635, 920
Hong, J., Grindlay, J., van den Berg, M., Laycock, S., Koenig, X., Zhao, P., & Schlegel, E. 2005a, BAAS, 207, 18.104
Hong, J., van den Berg, M., Schlegel, E. M., Grindlay, J. E., Koenig, X., Laycock, S., & Zhao, P. 2005b, ApJ, 635, 907
Howell, S. B., Nelson, L. A., & Rappaport, S. 2001, ApJ, 550, 897
Hurley, J. R., Tout, C. A., & Pols, O. R. 2002, MNRAS, 329, 897
Iben, I., Jr., Tutukov, A. V., & Yungelson, L. R. 1995, ApJS, 100, 233
in't Zand, J. J. M. 2005, A&A, 441, L1
Kent, S. M., Dame, T. M., & Fazio, G. 1991, ApJ, 378, 131
King, A. R. 2000, MNRAS, 315, L33
King, A. R., Ricketts, M. J., & Warwick, R. S. 1979, MNRAS, 187, P77
Kong, A. K. H., McClintock, J. E., Garcia, M. R., Murray, S. S., & Barret, D. 2002, ApJ, 570, 277
Krabbe, A., et al. 1995, ApJ, 447, L95
Kraft, R. P., Burrows, D. N., & Nousek, J. A. 1991, ApJ, 374, 344
Launhardt, R., Zylka, R., & Mezger, P. G. 2002, A&A, 384, 112
Law, C., & Yusef-Zadeh, F. 2004, ApJ, 611, 858
Laycock, S., Grindlay, J., van den Berg, M., Zhao, P., Hong, J., Koenig, X., Schlegel, E. M., & Persson, S. E. 2005, ApJ, 634, L53
Liu, Q. Z., van Paradijs, J., & van den Heuvel, E. P. J. 2001, A&A, 368, 1021
Liu, X. W., & Li, X. D. 2006, A&A, 449, 135
Lu, F. J., Wang, Q. D., & Lang, C. C. 2003, AJ, 126, 319
Lyons, L. 1991, A Practical Guide to Data Analysis for Physical Science Students (Cambridge: Cambridge Univ. Press)
Manners, J. C., et al. 2003, MNRAS, 343, 293
Martí, J., Mirable, I. F., Chaty, S., & Rodríguez, L. F. 2000, A&A, 363, 184
McNamara, D. H., Madsen, J. B., Barnes, J., & Ericksen, B. F. 2000, PASP, 112, 202
Muno, M. P., Bower, G. C., Burgasser, A. J., Baganoff, F. K., Morris, M. R., & Brandt, W. N. 2006, ApJ, 638, 183
Muno, M. P., Pfahl, E., Baganoff, F. K., Brandt, W. N., Ghez, A., Lu, J., & Morris, M. R. 2005, ApJ, 622, L113
Muno, M. P., et al. 2003, ApJ, 589, 225
———. 2004, ApJ, 613, 1179
Murdoch, H. S., Crawford, D. F., & Jauncey, D. 1973, ApJ, 183, 1
Patterson, J. 1984, ApJS, 54, 443
Pavlinsky, M. N., Grebenev, S. A., & Sunyaev, R. A. 1994, ApJ, 425, 110
Pfahl, E., Rappaport, S., & Podsiadlowski, P. 2002, ApJ, 571, L37
Pollock, A. M. T. 1987, ApJ, 320, 283
Porquet, D., Rodriguez, J., Corbel, S., Goldoni, P., Warwick, R. S., Goldwurm, A., & Decourchelle, A. 2003, A&A, 406, 299
Predehl, P., & Truemper, J. 1994, A&A, 290, L29
Ruiter, A. J., Belczynski, K., & Harrison, T. E. 2006, ApJ, 640, L167
Sakano, M., Koyama, K., Murakami, H., Maeda, Y., & Yamauchi, S. 2002, ApJS, 138, 19
Sakano, M., Warwick, R. S., Decourchelle, A., & Wang, Q. D. 2005, MNRAS, 357, 1211
Sazonov, S., Revnivtsev, M., Gilfanov, M., Churazon, E., & Sunyaev, R. 2006, A&A, 450, 117
Sidoli, L., Belloni, T., & Mereghetti, S. 2001, A&A, 368, 835
Sidoli, L., Mereghetti, S., Israel, G. L., Chiappetti, L., Treves, A., & Orlandini, M. 1999, ApJ, 525, 215
Suleimanov, V., Revnivtsev, M., & Ritter, H. 2005, A&A, 435, 191
Takagi, S., Murakami, H., & Koyama, K. 2002, ApJ, 573, 275
Townsley, L. K., Broos, P. S., Nousek, J. A., & Garmire, G. P. 2002, Nucl. Instrum. Methods Phys. Res. A, 486, 751
Ueda, Y., et al. 1999, ApJ, 518, 656
Verbunt, F., Bunk, W. H., Ritter, H., & Pfeffermann, E. 1997, A&A, 327, 602
Wang, Q. D. 2004, ApJ, 612, 159
Wang, Q. D., Gotthelf, E. V., & Lang, C. C. 2002, Nature, 415, 148
Watson, M. G., Willingale, R., Hertz, P., & Grindlay, J. E. 1981, ApJ, 250, 142
Weisskopf, M. C., Brinkman, B., Canizares, C., Garmire, G., Murray, S., & van Speybroeck, L. P. 2002, PASP, 114, 1
Wijnands, R., Guainazzi, M., van der Klis, M., & Méndez, M. 2002a, ApJ, 573, L45
Wijnands, R., Miller, J. M., & Wang, Q. D. 2002b, ApJ, 579, 422
Wijnands, R., & Wang, Q. D. 2002, ApJ, 568, L93
Wijnands, R., et al. 2006, A&A, 449, 1117
Yusef-Zadeh, F., Hewitt, J. W., & Cotton, W. 2004, ApJS, 155, 421
Yusef-Zadeh, F., Law, C., Wardle, M., Wang, Q. D., Fruscione, A., Lang, C. C., & Cotera, A. 2002, ApJ, 570, 665